Numerical investigation of the meshless radial basis integral equation method for solving 2D anisotropic potential problems

Ean Hin Ooi[1], Ean Tat Ooi[2], Whye Teong Ang[3]

[1]*School of Engineering, Monash University Malaysia, Bandar Sunway, 47500 Selangor, Malaysia*
[2]*School of Science, Information Technology and Engineering, Federation University, Ballarat, Victoria 3353, Australia*
[3]*School of Mechanical and Aerospace Engineering, Nanyang Technological University, 639798 Singapore*

Abstract

The radial basis integral equation (RBIE) method is derived for the first time to solve potential problems involving material anisotropy. The coefficients of the anisotropic conductivity require the gradient term to be modified accordingly when deriving the boundary integral equation so that the flux expression can be properly accounted. Analyses of the behaviour of the anisotropic fundamental solution and its spatial gradients showed that their variations along the subdomain boundaries may be large and they increase as the diagonal components of the material anisotropy become larger. The accuracy of the anisotropic RBIE was found to depend primarily on the accuracy of the influence coefficients evaluations and this precedes the number of nodes used. Root mean squared errors of less than 10^{-4}% can be obtained if evaluations of the influence coefficients are sufficiently accurate. An alternative formulation of the anisotropic RBIE was derived. The levels of accuracy obtained were not significantly different from the standard formulation.

Keywords: meshless method, anisotropy, integral equation, radial basis functions, RBIE

This is an early draft of the paper published in:
***Engineering Analysis with Boundary Elements* 53 (2015) 27-39.**

Author for correspondence: ooi.ean.hin@monash.edu (EH Ooi)

1. Introduction

Material anisotropy is encountered in many engineering problems such as groundwater flow, transport in biological media, composite materials, nanotechnology and more recently, transformation thermodynamics [1-4]. In many of these problems, analytical solutions are limited to only a few idealized cases. As a result, numerical techniques are often used to obtain approximate solutions. Discretization techniques such as the finite element method (FEM) and the boundary element method (BEM) are well-established and have been widely used for this purpose. Meshless methods on the other hand, belong to a class of numerical methods that do not involve discretization of the solution domain. Instead, these methods require only the distribution of collocation nodes, thus offering greater freedom and flexibility in terms of how the system matrix is set up during the numerical analysis.

Of particular interest in this paper is the radial basis integral equation (RBIE) method, which is an integral equation-based meshless method introduced by Popov and Bui [5]. The RBIE is unique because it solves simultaneously for each node, the unknown potential and its spatial gradients [6]. Consequently, the computation of the derivatives of shape functions such as that required by other numerical methods, for example FEM, is not necessary. The RBIE has been successfully implemented to solve various engineering problems and its versatility as an efficient and accurate numerical technique is well proven [6-9]. Nevertheless, the problems considered in these studies were confined to isotropic bodies. Problems involving material anisotropy have so far, remain unexplored.

In this paper, the RBIE is derived for the first time to solve problems in anisotropic media. The coefficients of the anisotropic conductivity give rise to vector-based flux terms. Therefore, some additional steps are required when deriving the integral equations for the implementation of the RBIE. Results from numerical experiments revealed that the stability and the accuracy of the numerical method depend on the strength of the material anisotropy. As a result, the anisotropic RBIE behaved differently from the isotropic RBIE when computational parameters, such as the number of nodes, the number of Gauss points and the size of the subdomains, were varied. This paper presents a numerical investigation into the optimum computational parameters of the RBIE when solving anisotropic problems. To maintain conciseness of the paper, only anisotropic potential problems will be considered. Many engineering problems are governed by the potential equation, for instance heat conduction and groundwater flow. Consequently, the numerical method presented in this paper provides an alternative to how these problems can be solved numerically.

This paper is organized into seven sections. The mathematical formulations of the RBIE for solving anisotropic potential problems are presented in Section 2. Section 3 outlines the implementation of the numerical method, while Section 4 examines the effects of material anisotropy on the influence coefficients of the RBIE. In Section 5, the anisotropic RBIE is used to solve several test problems, where its accuracy is tested and validated against analytical benchmarks. Discussions and conclusions are presented in Sections 6 and 7, respectively.

2. Mathematical formulations

2.1 The problem

Consider a two-dimensional homogeneous and anisotropic domain Ω bounded by the closed surface Γ. The anisotropic potential equation defined across this domain is given by:

$$\nabla \cdot \left(\mathbf{k} \nabla u(x_1, x_2)\right) = 0, \quad \text{for } (x_1, x_2) \in \Omega, \tag{1}$$

where (x_1,x_2) are the coordinates in the two-dimensional Cartesian system, u is potential and $\mathbf{k}$ is a second order tensor with Cartesian components k_{ij} (for i,j = 1, 2) where the strict conditions $k_{12} = k_{21}$ and $k_{11}k_{22} - (k_{12})^2 > 0$ apply. Depending on the type of problem, k_{ij} may stand for different material property. For instance, $\mathbf{k}$ can represent the anisotropic thermal conductivity in heat conduction and the anisotropic hydraulic conductivity in groundwater flow. The following boundary conditions are prescribed:

$$u(x_1, x_2) = u_o(x_1, x_2), \quad \text{for } (x_1, x_2) \in \Gamma_1, \tag{2a}$$

$$\frac{\partial u(x_1, x_2)}{\partial n^+} = q_o(x_1, x_2), \quad \text{for } (x_1, x_2) \in \Gamma_2 \tag{2b}$$

where u_o and q_o are suitably prescribed functions of (x_1,x_2), Γ_1 and Γ_2 are non-intersecting parts of Γ such that $\Gamma_1 \cup \Gamma_2 = \Gamma$ and $\partial/\partial n^+$ is the vector differential operator given by:

$$\frac{\partial}{\partial n^+} = \sum_{i,j=1}^{2} k_{ij} n_i(x_1, x_2) \frac{\partial}{\partial x_j}, \tag{3}$$

where n_i is the outward unit normal vector in the x_i direction at point (x_1,x_2). We seek the solution of Eq. (1) subject to the boundary conditions in Eqs. (2a) and (2b).

2.2 The anisotropic radial basis integral equation method

To carry out the RBIE, a series of N_t collocation nodes are distributed along the boundary and within the interior of the solution domain, see Figure 1(a). A circular subdomain denoted by $\Omega_i \cup \Gamma_i$ (for i = 1, 2, …, $N_t - 1$, N_t) centred at each node is generated. These circles may be of different radii, may overlap and may extend beyond the boundary of the solution domain, as shown in Figure 1(b). Once the collocation nodes and their respective subdomains are generated, an integral form of Eq. (1), which is valid in each subdomain $\Omega_i \cup \Gamma_i$ is derived. Using the reciprocal theorem and the fundamental solution of the anisotropic Laplace equation [10], and making use of the relationship in Eq. (3), one obtains:

$$\begin{aligned} u(\xi_1^{(i)}, \xi_2^{(i)}) = \int_{\Gamma_i} \Bigg[& u(x_1, x_2)\Theta(x_1, x_2; \xi_1^{(i)}, \xi_2^{(i)}) - \kappa_1(x_1, x_2)\Phi(x_1, x_2; \xi_1^{(i)}, \xi_2^{(i)}) \frac{\partial u(x_1, x_2)}{\partial x_1} \\ & - \kappa_2(x_1, x_2)\Phi(x_1, x_2; \xi_1^{(i)}, \xi_2^{(i)}) \frac{\partial u(x_1, x_2)}{\partial x_2} \Bigg] \mathrm{d}s(x_1, x_2), \end{aligned} \tag{4}$$

where $(\xi_1^{(i)},\xi_2^{(i)})$ (for i = 1, 2, …, $N_t - 1$, N_t) are the source point coordinates, which are represented by the centre of the subdomain Ω_i, $\mathrm{d}s(x_1,x_2)$ is the infinitesimal length of the curve Γ_i and κ_1 and κ_2 are coefficients defined by:

$$\kappa_1(x_1, x_2) = n_1(x_1, x_2)k_{11} + n_2(x_1, x_2)k_{12}, \tag{5a}$$

$$\kappa_2(x_1, x_2) = n_1(x_1, x_2)k_{12} + n_2(x_1, x_2)k_{22}. \tag{5b}$$

$\Phi(x_1,x_2;\xi_1^{(i)},\xi_2^{(i)})$ and $\Theta(x_1,x_2;\xi_1^{(i)},\xi_2^{(i)})$ in Eq. (4) are the anisotropic fundamental solution of the Laplace equation and its normal derivative, respectively, which can be expressed as [11]:

$$\Phi(x_1,x_2;\xi_1,\xi_2)=\frac{|s_{ij}|^{\frac{1}{2}}}{4\pi}\ln\left[s_{11}(x_1-\xi_1)^2+2s_{12}(x_1-\xi_1)(x_2-\xi_2)+s_{22}(x_2-\xi_2)^2\right], \tag{6a}$$

$$\Theta(x_1,x_2;\xi_1,\xi_2)=\frac{|s_{ij}|^{\frac{1}{2}}}{4\pi}\left[\kappa_1(x_1,x_2)\frac{\partial\Phi(x_1,x_2;\xi_1,\xi_2)}{\partial x_1}+\kappa_2(x_1,x_2)\frac{\partial\Phi(x_1,x_2;\xi_1,\xi_2)}{\partial x_2}\right], \tag{6b}$$

where s_{ij} is the inverse of the matrix k_{ij} and $|.|$ is the determinant.

The fundamental solution and its normal derivative in Eqs. (6a) and (6b) are different from those of the isotropic case due to the presence of the anisotropic conductivity tensor k_{ij}, which is here expressed in terms of its inverse s_{ij}. Therefore, the material anisotropy can influence the variation of the fundamental solution and its normal derivative along the subdomain boundary. This will be examined in Section 4.

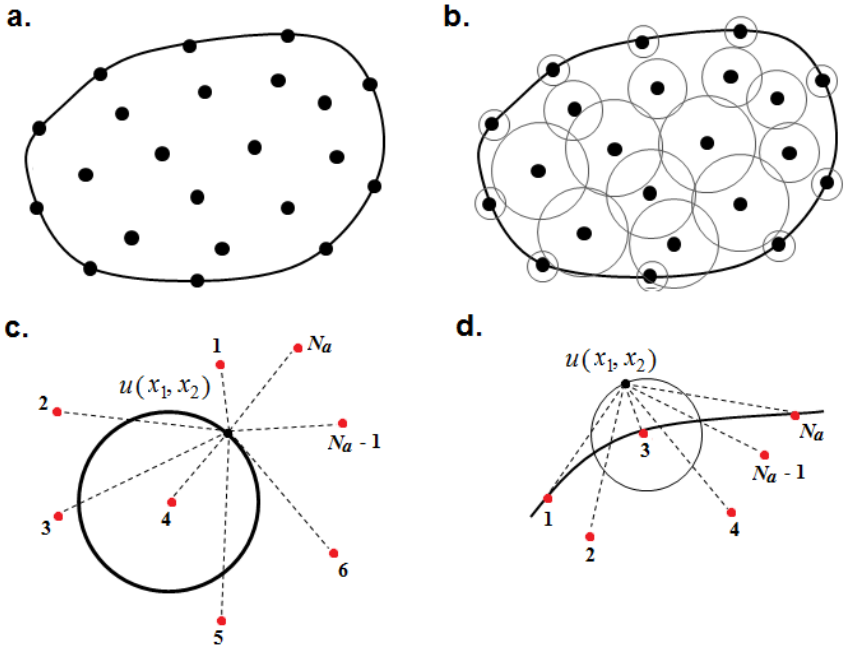

Figure 1: (a) Distribution of collocation nodes, (b) generation of circular subdomains, (c) interpolation of field variables, and (d) extrapolation of field variables.

As pointed out in Section 1, the RBIE solves simultaneously for the unknown potential and its spatial gradients at each node. Therefore, two additional equations are required in order to complete the formulation. These equations are obtained by differentiating Eq. (4) with respect to the source point coordinate, ξ_1 and ξ_2. This results in [6]:

$$\frac{\partial u^{(i)}}{\partial\xi_1}=\int_{\Gamma_i}\left[u\frac{\partial\Theta^{(i)}}{\partial\xi_1}-\kappa_1\frac{\partial\Phi^{(i)}}{\partial\xi_1}\frac{\partial u}{\partial x_1}-\kappa_2\frac{\partial\Phi^{(i)}}{\partial\xi_1}\frac{\partial u}{\partial x_2}\right]\mathrm{d}s, \tag{7}$$

and

$$\frac{\partial u^{(i)}}{\partial\xi_2}=\int_{\Gamma_i}\left[u\frac{\partial\Theta^{(i)}}{\partial\xi_2}-\kappa_1\frac{\partial\Phi^{(i)}}{\partial\xi_2}\frac{\partial u}{\partial x_1}-\kappa_2\frac{\partial\Phi^{(i)}}{\partial\xi_2}\frac{\partial u}{\partial x_2}\right]\mathrm{d}s. \tag{8}$$

where the terms indicating spatial dependence have been dropped for simplicity. The complete expressions of $\partial\Phi/\partial\xi_i$ and $\partial\Theta/\partial\xi_i$ are given in Appendix A.

In the RBIE, the field variables $u(x_1,x_2)$, $\partial u(x_1,x_2)/\partial x_1$ and $\partial u(x_1,x_2)/\partial x_2$ in Eqs. (4), (7) and (8) are approximated based on values of the surrounding nodes using radial basis function (RBF) interpolations, see Figure 1(c). For added numerical stability, these interpolations are usually augmented with global polynomials [12]. Therefore:

$$u(x_1,x_2) \approx \sum_{k=1}^{N_a} f(x_1,x_2;x_1^{(k)},x_2^{(k)})a_1^{(k)} + \sum_{m=1}^{N_m} b_1^{(m)} p(x_1,x_2;x_1^{(m)},x_2^{(m)}), \tag{9a}$$

$$\frac{\partial u(x_1,x_2)}{\partial x_1} \approx \sum_{k=1}^{N_a} f(x_1,x_2;x_1^{(k)},x_2^{(k)})a_2^{(k)} + \sum_{m=1}^{N_m} b_2^{(m)} p(x_1,x_2;x_1^{(m)},x_2^{(m)}), \tag{9b}$$

$$\frac{\partial u(x_1,x_2)}{\partial x_2} \approx \sum_{k=1}^{N_a} f(x_1,x_2;x_1^{(k)},x_2^{(k)})a_3^{(k)} + \sum_{m=1}^{N_m} b_3^{(m)} p(x_1,x_2;x_1^{(m)},x_2^{(m)}), \tag{9c}$$

where $f(x_1,x_2;x_1^{(k)},x_2^{(k)})$ is the RBF, N_a is the number of points used in the interpolation, N_m is the number of terms contained in the polynomial $p(x_1,x_2;x_1^{(m)},x_2^{(m)})$, which has the same order as the RBF [12] and a_i, b_i (for i = 1, 2 and 3) are unknown coefficients that are determined by collocating Eqs. (9a) to (9c) at the N_a interpolation points. This results in three system matrices, each corresponding to Eqs. (9a), (9b) and (9c), that can be inverted to give:

$$\begin{bmatrix}\mathbf{a}_1\\ \mathbf{b}_1\end{bmatrix} = \begin{bmatrix}\mathbf{F} & \mathbf{P}\\ \mathbf{P}^T & \mathbf{0}\end{bmatrix}^{-1}\begin{bmatrix}\mathbf{u}\\ \mathbf{0}\end{bmatrix},\quad \begin{bmatrix}\mathbf{a}_2\\ \mathbf{b}_2\end{bmatrix} = \begin{bmatrix}\mathbf{F} & \mathbf{P}\\ \mathbf{P}^T & \mathbf{0}\end{bmatrix}^{-1}\begin{bmatrix}\partial\mathbf{u}/\partial x_1\\ \mathbf{0}\end{bmatrix},\quad \begin{bmatrix}\mathbf{a}_3\\ \mathbf{b}_3\end{bmatrix} = \begin{bmatrix}\mathbf{F} & \mathbf{P}\\ \mathbf{P}^T & \mathbf{0}\end{bmatrix}^{-1}\begin{bmatrix}\partial\mathbf{u}/\partial x_2\\ \mathbf{0}\end{bmatrix}, \tag{10}$$

where $\mathbf{u} = u^{(k)}$, $\partial\mathbf{u}/\partial x_1 = \partial u^{(k)}/\partial x_1$ and $\partial\mathbf{u}/\partial x_2 = \partial u^{(k)}/\partial x_2$ (for k = 1, 2,…, N_a). Substituting Eq. (10) into (9) leads to:

$$u(x_1,x_2) \approx \left[\mathbf{F}(x_1,x_2;x_1^{(k)},x_2^{(k)}) \quad \mathbf{P}(x_1;x_2)\right]\mathbf{A}^{-1}\begin{bmatrix}\mathbf{u}\\ \mathbf{0}\end{bmatrix}, \tag{11a}$$

$$\frac{\partial u(x_1,x_2)}{\partial x_1} \approx \left[\mathbf{F}(x_1,x_2;x_1^{(k)},x_2^{(k)}) \quad \mathbf{P}(x_1;x_2)\right]\mathbf{A}^{-1}\begin{bmatrix}\partial\mathbf{u}_1\\ \mathbf{0}\end{bmatrix}, \tag{11b}$$

$$\frac{\partial u(x_1,x_2)}{\partial x_2} \approx \left[\mathbf{F}(x_1,x_2;x_1^{(k)},x_2^{(k)}) \quad \mathbf{P}(x_1;x_2)\right]\mathbf{A}^{-1}\begin{bmatrix}\partial\mathbf{u}_2\\ \mathbf{0}\end{bmatrix} \tag{11c}$$

where

$$\mathbf{A} = \begin{bmatrix}\mathbf{F} & \mathbf{P}\\ \mathbf{P}^T & \mathbf{0}\end{bmatrix}.$$

For the nodes that are located at the global boundary, part of the subdomain is outside of Ω, as shown in Figure 1(b). In this case, the RBF approximations defined in Eqs. (9) to (11) are still applicable; the unknown field variables are now extrapolated based on the values at the nearby nodes located within the solution domain, see Figure 1(d).

Substituting Eqs. (9), (10) and (11) into (4), (7) and (8) and expressing the resulting equations in matrix notation yields:

$$u^{(i)} = \mathbf{H}^{(i)}\{\mathbf{u}\} - \mathbf{G}_1^{(i)}\{\frac{\partial \mathbf{u}}{\partial x_1}\} - \mathbf{G}_2^{(i)}\{\frac{\partial \mathbf{u}}{\partial x_2}\}, \tag{12}$$

$$\frac{\partial u^{(i)}}{\partial \xi_1} = \frac{\partial \mathbf{H}^{(i)}}{\partial \xi_1}\{\mathbf{u}\} - \frac{\partial \mathbf{G}_1^{(i)}}{\partial \xi_1}\{\frac{\partial \mathbf{u}}{\partial x_1}\} - \frac{\partial \mathbf{G}_2^{(i)}}{\partial \xi_1}\{\frac{\partial \mathbf{u}}{\partial x_2}\}, \tag{13}$$

and

$$\frac{\partial u^{(i)}}{\partial \xi_2} = \frac{\partial \mathbf{H}^{(i)}}{\partial \xi_2}\{\mathbf{u}\} - \frac{\partial \mathbf{G}_1^{(i)}}{\partial \xi_2}\{\frac{\partial \mathbf{u}}{\partial x_1}\} - \frac{\partial \mathbf{G}_2^{(i)}}{\partial \xi_2}\{\frac{\partial \mathbf{u}}{\partial x_2}\}, \tag{14}$$

where $\mathbf{H}$, $\mathbf{G}_1$, $\mathbf{G}_2$ and their derivatives with respect to ξ_1 and ξ_2 are known as the influence coefficients of the anisotropic RBIE. The explicit terms of $\mathbf{H}$, $\mathbf{G}_1$ and $\mathbf{G}_2$ are:

$$\begin{aligned}\mathbf{H}^{(i)} = &\sum_{k=1}^{N_a} A_{k,i}^{-1} \int_{\Gamma_i} f(x_1, x_2; x_1^{(k)}, x_2^{(k)}) \Theta(x_1, x_2; \xi_1^{(i)}, \xi_2^{(i)}) \mathrm{d}s(x_1, x_2) \\ &+ \sum_{m=1}^{N_m} A_{m+N_a,i}^{-1} \int_{\Gamma_i} p(x_1, x_2; x_1^{(m)}, x_2^{(m)}) \Theta(x_1, x_2; \xi_1^{(i)}, \xi_2^{(i)}) \mathrm{d}s(x_1, x_2),\end{aligned} \tag{15a}$$

$$\begin{aligned}\mathbf{G}_1^{(i)} = &\sum_{k=1}^{N_a} A_{k,i}^{-1} \int_{\Gamma_i} f(x_1, x_2; x_1^{(k)}, x_2^{(k)}) \kappa_1(x_1, x_2) \Phi(x_1, x_2; \xi_1^{(i)}, \xi_2^{(i)}) \mathrm{d}s(x_1, x_2) \\ &+ \sum_{m=1}^{N_m} A_{m+N_a,i}^{-1} \int_{\Gamma_i} p(x_1, x_2; x_1^{(m)}, x_2^{(m)}) \kappa_1(x_1, x_2) \Phi(x_1, x_2; \xi_1^{(i)}, \xi_2^{(i)}) \mathrm{d}s(x_1, x_2),\end{aligned} \tag{15b}$$

$$\begin{aligned}\mathbf{G}_2^{(i)} = &\sum_{k=1}^{N_a} A_{k,i}^{-1} \int_{\Gamma_i} f(x_1, x_2; x_1^{(k)}, x_2^{(k)}) \kappa_2(x_1, x_2) \Phi(x_1, x_2; \xi_1^{(i)}, \xi_2^{(i)}) \mathrm{d}s(x_1, x_2) \\ &+ \sum_{m=1}^{N_m} A_{m+N_a,i}^{-1} \int_{\Gamma_i} p(x_1, x_2; x_1^{(m)}, x_2^{(m)}) \kappa_2(x_1, x_2) \Phi(x_1, x_2; \xi_1^{(i)}, \xi_2^{(i)}) \mathrm{d}s(x_1, x_2).\end{aligned} \tag{15c}$$

Eqs. (12), (13) and (14) along with the boundary conditions precscribed, when applied to all the collocation nodes, set up a system of equations that can be solved for the unknown u, $\partial u/\partial x_1$ and $\partial u/\partial x_2$ at each node.

The anisotropic RBIE formulated above, which solves for the potential and its spatial gradients, is referred to in this paper as the standard formulation. It is possible to formulate the anisotropic RBIE differently such that it solves for the potential and the components of fluxes. The derivation of this different formulation, which is hereafter referred to as the alternative formulation, is presented in Appendix B. We shall restrict our investigations in this paper to the standard formulation. The accuracy and merits of the alternative formulation will be discussed in Section 6.

3. Numerical procedure

3.1 Implementation

To implement the anisotropic RBIE, Eqs. (12), (13) and (14) are applied at the N_t collocation nodes. When the collocation node is inside the solution domain, u, $\partial u/\partial x_1$ and $\partial u/\partial x_2$ are unknowns. Hence, all three equations are used to set up the system of linear algebraic equations. When the collocation node is on the boundary where the Dirichlet condition is prescribed, Eqs. (13) and (14) are used to set up the system of equations since the potential at this node is known from the boundary condition. When the collocation node is at the boundary where the Neumann condition is prescribed, two cases are prevalent. To illustrate the implementation for each case, consider the definition of the flux in an anisotropic medium given by Eq. (3). Expanding Eq. (3) and rearranging the terms gives:

$$\frac{\partial u}{\partial n^+} = (k_{11}n_1 + k_{12}n_2)\frac{\partial u}{\partial x_1} + (k_{12}n_1 + k_{22}n_2)\frac{\partial u}{\partial x_2} \equiv \kappa_1 \frac{\partial u}{\partial x_1} + \kappa_2 \frac{\partial u}{\partial x_2}. \tag{16}$$

In the case where $|\kappa_1| > |\kappa_2|$, Eqs. (12) and (14) are used to set up the system matrix. The variable $\partial u/\partial x_1$ is eliminated from the equations by using the relationship in Eq. (16). When $|\kappa_2| > |\kappa_1|$, Eqs. (12) and (13) are used instead, with $\partial u/\partial x_2$ eliminated from these equations using Eq. (16).

3.2 Selection of interpolation points

The two approaches outlined by Popov and Bui [5] may be used to select the interpolation points in the RBF approximations. In the first approach, a fictitious circle with a pre-defined radius centred at the collocated node is generated. The nodes that lie inside the fictitious circle are then selected for the RBF interpolation. In the second approach, the N_a points closest to the collocated node are selected. The second approach is usually preferred since it ensures that every node employs the same number of interpolation points. While this is not necessary a criterion for implementing the RBIE, it is computationally more convenient and shall be adopted in this paper.

3.3 Selection of subdomain radius

When implementing the *isotropic* RBIE, the radius of the subdomain for the node at the interior is usually chosen to be the same as the distance to the nearest node. This is optimal for producing numerical results that are stable and accurate [13]. For the subdomains that are centred on the nodes at the global boundary, the radius is chosen to be 0.1 times the distance to the nearest node. This is to minimize the error due to extrapolation of the field variables that are exterior to the solution domain [5].

The conditions above, which are optimal for isotropic RBIE [13], may not be ideal for the anisotropic problems considered here. As shall be demonstrated in Section 4, the variations of the fundamental solution and its spatial derivatives depend on the size of the subdomain. Consequently, the choice of 0.1 times the smallest distance between nodes for the boundary subdomain may introduce significant error especially when the number of nodes is increased. In the subsequent studies, numerical investigations are carried out to determine the optimum radii for the interior and boundary subdomains when solving anisotropic problems.

3.4 Choice of radial basis functions

The choice of which RBF to use is an open question. Various RBFs are available to carry out the interpolation of the field variables in Eq. (9). A good choice is one that can produce accurate numerical solutions and is independent of the computational parameters and the type of problems. Ooi and Popov [6] investigated the performance of the first and second order polyharmonic splines when solving isotropic problems using the RBIE and concluded that the second order spline of the form:

$$f(x_1, x_2; x_1^{(k)}, x_2^{(k)}) = r^4(x_1, x_2; x_1^{(k)}, x_2^{(k)}) \log[r(x_1, x_2; x_1^{(k)}, x_2^{(k)})], \tag{17}$$

produced results that are more accurate than its first order counterpart. The parameter $r(x_1,x_2;x_1^{(k)},x_2^{(k)})$ is the Euclidean distance between the points (x_1,x_2) and $(x_1^{(k)},x_2^{(k)})$. More recently, Ooi and Popov [14] employed the third order polyharmonic spline of the form:

$$f(x_1, x_2; x_1^{(k)}, x_2^{(k)}) = r^6(x_1, x_2; x_1^{(k)}, x_2^{(k)}) \log[r(x_1, x_2; x_1^{(k)}, x_2^{(k)})], \tag{18}$$

to solve incompressible flow problems. They found that the third order spline is important to ensure convergence when the problem has a high degree of nonlinearity.

Other RBFs that have been used by researchers include the multiquadrics [15, 16] and the Gaussian function [17], which are known to yield very accurate results. However, these RBFs contain a free parameter, which has an optimal value that depends on the type of problem solved, the distribution of nodes and the precision of the computation [18]. Although various algorithms exist that help to determine the optimal free parameter, they are mostly tailored for solving partial differential equations and not for approximating field variables.

In this paper, we extend the work of Ooi and Popov [6, 14] by investigating the accuracies of the anisotropic RBIE when implemented with the second and third order polyharmonic splines (see Eqs. (17) and (18)). The global polynomial $p(x_1,x_2)$ associated with these RBFs (see Eq. (9)) have the same order as the RBFs and are given by $p(x_1,x_2) = 1 + x_1 + x_2 + x_1^2 + x_1x_2 + x_2^2$ for the second order RBF and $p(x_1,x_2) = 1 + x_1 + x_2 + x_1^2 + x_1x_2 + x_2^2 + x_1^3 + x_1^2x_2 + x_1x_2^2 + x_2^3$ for the third order RBF.

3.5 Effects of geodesic distance

The term $r(x_1,x_2;x_1^{(k)},x_2^{(k)})$ in Eqs. (17) and (18) refers to the Euclidean distance between two points. When the problem is anisotropic, the coefficients of the conductivity tensor have the capacity to 'virtually stretch' the dimensions of the solution domain. In order to help the numerical scheme cope with this, it is more feasible to adopt the geodesic distance, i.e.:

$$r(x_1, x_2; x_1^{(k)}, x_2^{(k)}) = \sqrt{s_{11}(x_1 - x_1^{(k)})^2 + 2s_{12}(x_1 - x_1^{(k)})(x_2 - x_2^{(k)}) + s_{22}(x_2 - x_2^2)^2}, \tag{19}$$

instead of the Euclidean distance when implementing the RBF interpolations. These RBFs, which are defined by the geodesic distance, were used by Ang et al. [19] in their implementation of the dual reciprocity boundary element method for analysing non-homogeneous anisotropic materials. One may notice that the square of the geodesic distance in Eq. (19) is identical to the expression inside the logarithm in Eq. (6a).

4. Effects of material anisotropy on the influence coefficients

Chang et al. [11] reported that the ease of which anisotropic potential problems can be solved depends on the determinant of the anisotropic tensor, i.e. $|k_{ij}| = k_{11}k_{22} - (k_{12})^2$. A smaller $|k_{ij}|$ yields a more asymmetrical potential distribution, hence increasing the difficulty in obtaining a numerical solution. From Eq. (6), one may observe that Θ, $\kappa_1\Phi$, $\kappa_2\Phi$, $\partial\Theta/\partial\xi_1$, $\kappa_1\partial\Phi/\partial\xi_1$, $\kappa_2\partial\Phi/\partial\xi_1$, $\partial\Theta/\partial\xi_2$, $\kappa_1\partial\Phi/\partial\xi_2$ and $\kappa_2\partial\Phi/\partial\xi_2$ are expressed in terms of the anisotropic material tensor. Based on the argument of Chang et al. [11], it is reasonable to expect the integrals defined in Eq. (15) to become more difficult to compute as $|k_{ij}|$ becomes smaller. To investigate if this is true, we set $k_{11} = k_{22} = 1$ and examine the variations of Θ, $\kappa_1\Phi$, $\kappa_2\Phi$ and their spatial derivatives with respect to ξ_1 and ξ_2 along the subdomain boundary for $0 < k_{12} < 1$. A similar argument applies for the same terms defined in Eqs. (A2) – (A9) in Appendix A.

Figure 2 plots the values of Θ, $\kappa_1\Phi$, $\kappa_2\Phi$ and their spatial derivatives along the circumference of a circular subdomain $[0\ 2\pi]$ of radius 0.1. Results for the isotropic case ($k_{12} = 0$) are also plotted for comparison. The variations in the plots increase with the value of k_{12}. Likewise, the variations in the anisotropic cases are greater than their isotropic counterparts. From a numerical standpoint, the larger variations imply that the numerical integrals are more difficult to solve. Hence, more quadrature points are needed to solve more accurately the integrals in Eq. (15).

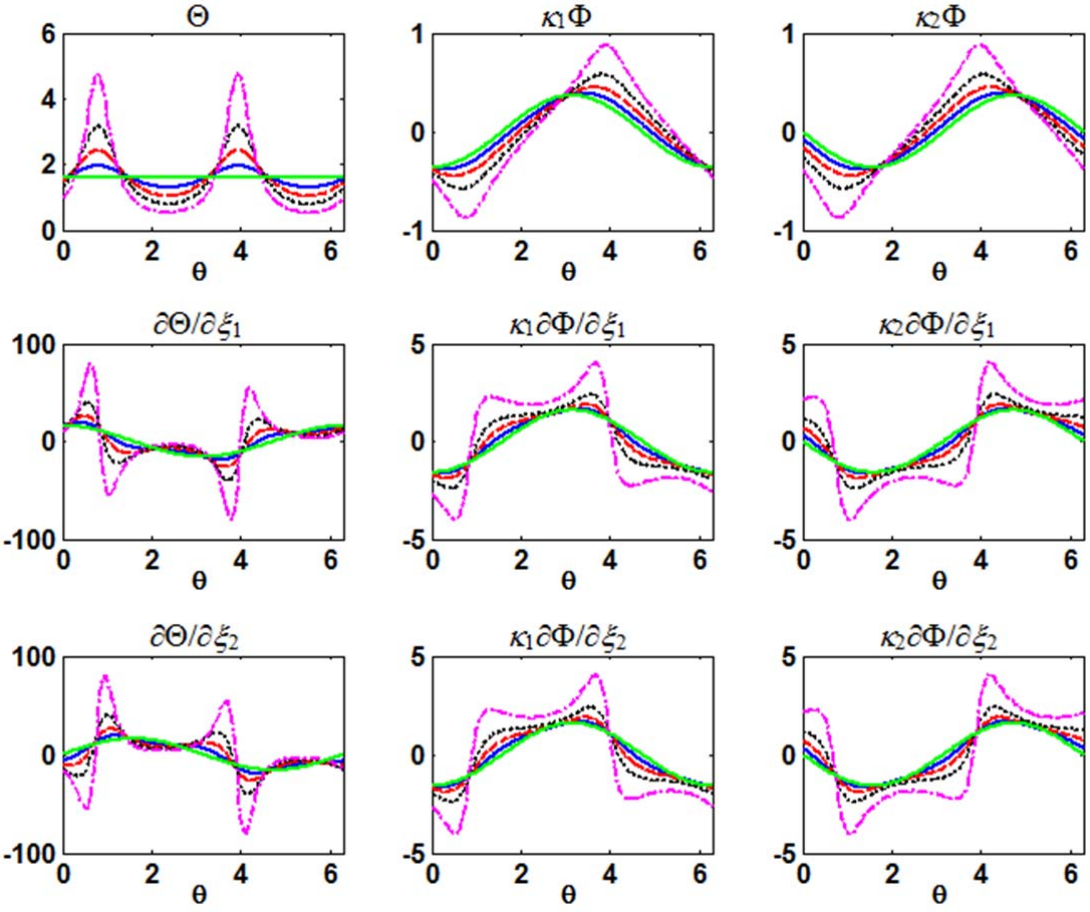

Figure 2: Plots of Θ, $\kappa_1\Phi$, $\kappa_2\Phi$ and their derivatives with respect to ξ_1 and ξ_2 along the circumference of the circular subdomain for k_{12} = 0.2 (solid blue), 0.4 (dashed red), 0.6 (dotted black), 0.8 (dotted-dashed purple) and 0 [isotropic] (solid green).

Next, we investigate the importance of the ratio k_{11}/k_{22} by choosing five values, namely k_{11}/k_{22} = 1, 2, 3, 4 and 5. The value of k_{12} and the subdomain radius in this case are set to zero and 0.1, respectively. Figure 3 plots the values of Θ, $\kappa_1\Phi$, $\kappa_2\Phi$ and their spatial derivatives along the circumference of a circular subdomain [0 2π]. As the ratio k_{11}/k_{22} increases, the variations of the plotted parameters increase; suggesting that the integrals defined in Eqs. (15a) to (15c) become more difficult to evaluate.

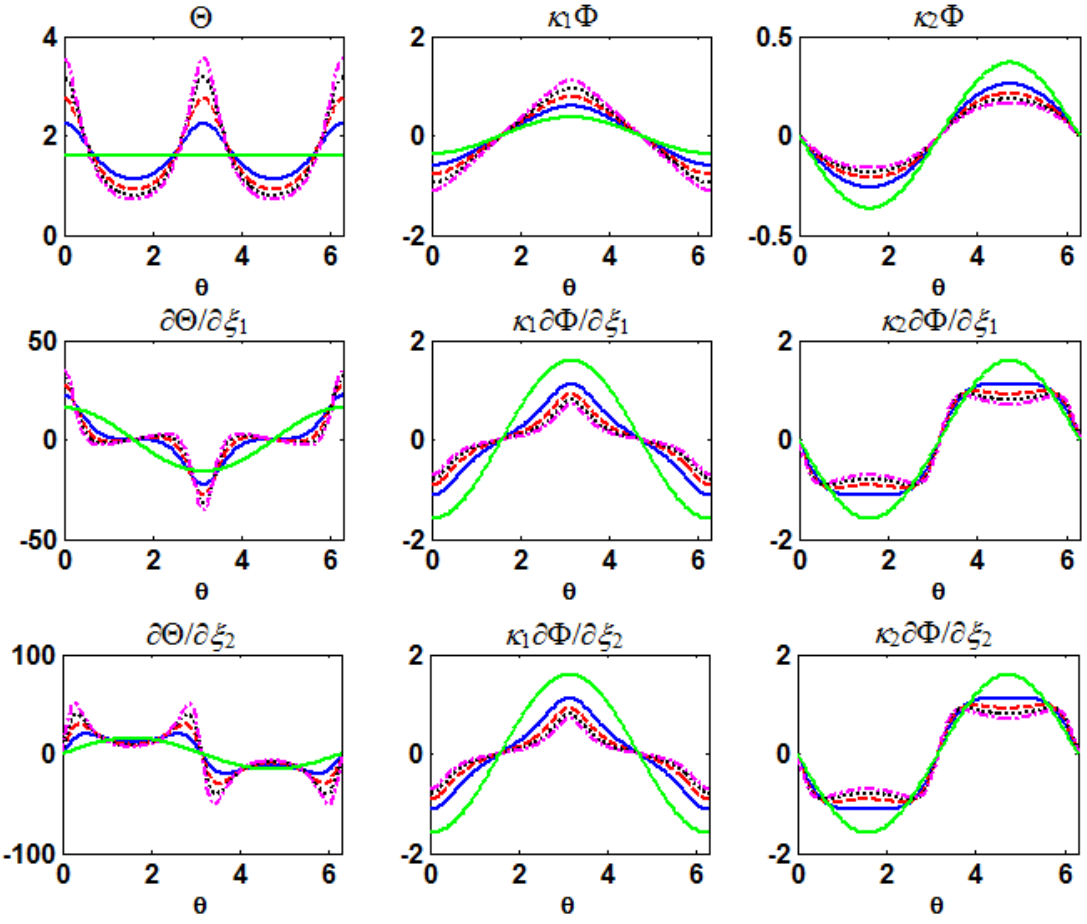

Figure 3: Plots of Θ, $\kappa_1\Phi$, $\kappa_2\Phi$ and their derivatives with respect to ξ_1 and ξ_2 along the circumference of the circular subdomain for k_{11}/k_{12} = 2 (solid blue), 3 (dashed red), 4 (dotted black), 5 (dotted-dashed purple) and 1 [isotropic] (solid green).

We also investigated the effects of the subdomain radius on the distribution of Θ, $\kappa_1\Phi$, $\kappa_2\Phi$ and their spatial derivatives. Since the subdomain radius was chosen to be equivalent to the distance to the nearest node (see Section 3), smaller subdomains imply the use of larger number of nodes. For this study, we set $k_{11} = k_{22} = 1$ and $k_{12} = 0.5$ and observe the responses of Θ, $\kappa_1\Phi$, $\kappa_2\Phi$, $\partial\Theta/\partial\xi_1$, $\kappa_1\partial\Phi/\partial\xi_1$, $\kappa_2\partial\Phi/\partial\xi_1$, $\partial\Theta/\partial\xi_2$, $\kappa_1\partial\Phi/\partial\xi_2$ and $\kappa_2\partial\Phi/\partial\xi_2$ for subdomain radii of 0.1, 0.05 and 0.025. The results are illustrated in Figure 4, where Θ, $\kappa_1\Phi$, $\kappa_2\Phi$ and their spatial derivatives were found to vary more greatly as the subdomain becomes smaller. As indicated earlier, this suggests that the integrals in Eq. (15) will become more difficult to solve.

From the analyses carried out in this section we have shown that in problems that are highly anisotropic, i.e. when k_{12} is large, increasing the number of nodes while maintaining the subdomain radius to be equivalent to the distance to the nearest node – as in the isotropic

case [6, 13] – may not necessarily yield more accurate numerical results *if* the evaluations of the integrals in Eq. (15) are not sufficiently accurate.

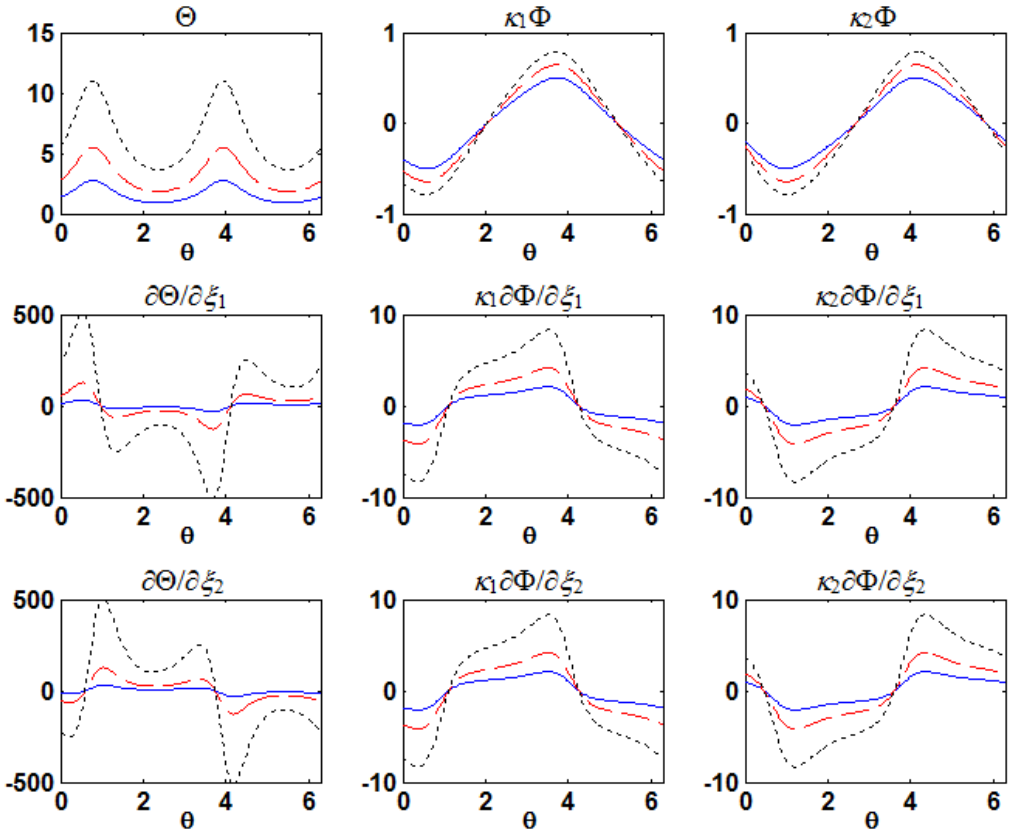

Figure 4: Plots of Θ, $\kappa_1\Phi$, $\kappa_2\Phi$ and their derivatives with respect to ξ_1 and ξ_2 along the circumference of the circular subdomain for radius of 0.1 (solid blue), 0.05 (dashed red) and 0.025 (dotted black).

5. Results

5.1 Test problem 1

We consider the unit square domain (x_1,x_2: [0, 1]) where the coefficients of the anisotropic conductivity are given by $k_{11} = 5$, $k_{22} = 1$ and $k_{12} = 2$. The Dirichlet condition:

$$u(x_1, x_2) = \frac{x_1^3}{5} - x_1^2 x_2 + x_1 x_2^2 + \frac{x_2^3}{3}, \tag{20}$$

is applied to all the boundaries. Eq. (20) also represents the analytical solution across the boundary and interior of the solution domain. In order to quantify the accuracy of the numerical scheme, we calculate the root mean squared (RMS) error e_{rms}:

$$e_{rms} = 100\% \times \frac{\sqrt{\sum_i (\phi_{ex}^{(i)} - \phi_{num}^{(i)})^2}}{n} \tag{21}$$

where ϕ can represent either u, $\partial u/\partial x_1$ or $\partial u/\partial x_2$, n is the total number of observations and the subscripts '*ex*' and '*num*' represent the exact and numerical values, respectively.

One of the benefits of using the RMS error is its capability to provide a rough indication on the level of accuracy of the numerical solutions [20]. Generally, the number of zeroes after the decimal in e_{rms} indicates the number of decimal places in the numerical values that are calculated correctly. For instance, an RMS error of 0.0001 suggests that the numerical solution is correct up to 3 decimal places.

In all the numerical results presented, the RBF interpolations were carried out using the second order polyharmonic splines, 25 points interpolation points and the RBF defined based on the geodesic distance (see Section 3.5). Numerical experiments indicated that increasing the number of interpolation points beyond 25 did not significantly improve the numerical solutions. The integrals in Eq. (15) were calculated numerically using the Gaussian quadrature. All numerical simulations were carried out using a laptop with Intel Core i3 (2.4GHz) processor and 4GB of memory.

5.1.1 Optimum subdomain radius

We examine first the optimum subdomain radius for solving anisotropic problems. Four values were considered, namely $0.5\delta x$, $1.0\delta x$, $1.5\delta x$ and $2.0\delta x$, where δx is the smallest distance between two adjacent nodes. For simplicity, we assume a uniform distribution of nodes so that δx is homogeneous across the solution domain. Three sets of nodes were considered: N_t = 121 (δx = 0.1), 441 (δx = 0.05) and 1681 (δx = 0.025). In order to minimize errors from the numerical integration, we employ 150 Gauss points to numerically evaluate Eq. (15). Figures 5a, 5b and 5c plots the contours of the RMS errors of u, $\partial u/\partial x_1$ and $\partial u/\partial x_2$, respectively against the different radii of interior (R_i) and boundary (R_b) subdomains. The contours of u, $\partial u/\partial x_1$ and $\partial u/\partial x_2$ obtained using δx = 0.05, $R_i = 1.0\delta x$ and $R_b = 0.1\delta x$ are shown in Figure 5d. The numerical solutions obtained when δx = 0.1 were unreliable, as indicated by the RMS error of the order of $O(-1)$. For the case when δx = 0.05, the optimum values of R_i and R_b were $1.5\delta x$ and $0.5\delta x$, respectively. With δx = 0.025, the corresponding optimum values became $2.0\delta x$ and $1.0\delta x$.

The differences in the optimum values for different δx are likely due to the dependence of the fundamental solution and its spatial derivatives (see Section 4) on the size of the subdomain, which is scaled according to δx. As δx becomes smaller, the variation of these functions become larger, thus necessitating the subdomains to be larger in order to give more accurate numerical solutions.

Nevertheless, it must be noted that except for the case where $R_i < 0.1$, there is very little difference in the order of RMS error obtained for the different combinations of R_i and R_b when δx = 0.025. This indicates that the numerical solutions are less sensitive to the variations in the subdomain radius. The large errors observed when $R_b = 2.0\delta x$ are due to extrapolation errors where a large part of the subdomain lie outside the solution domain.

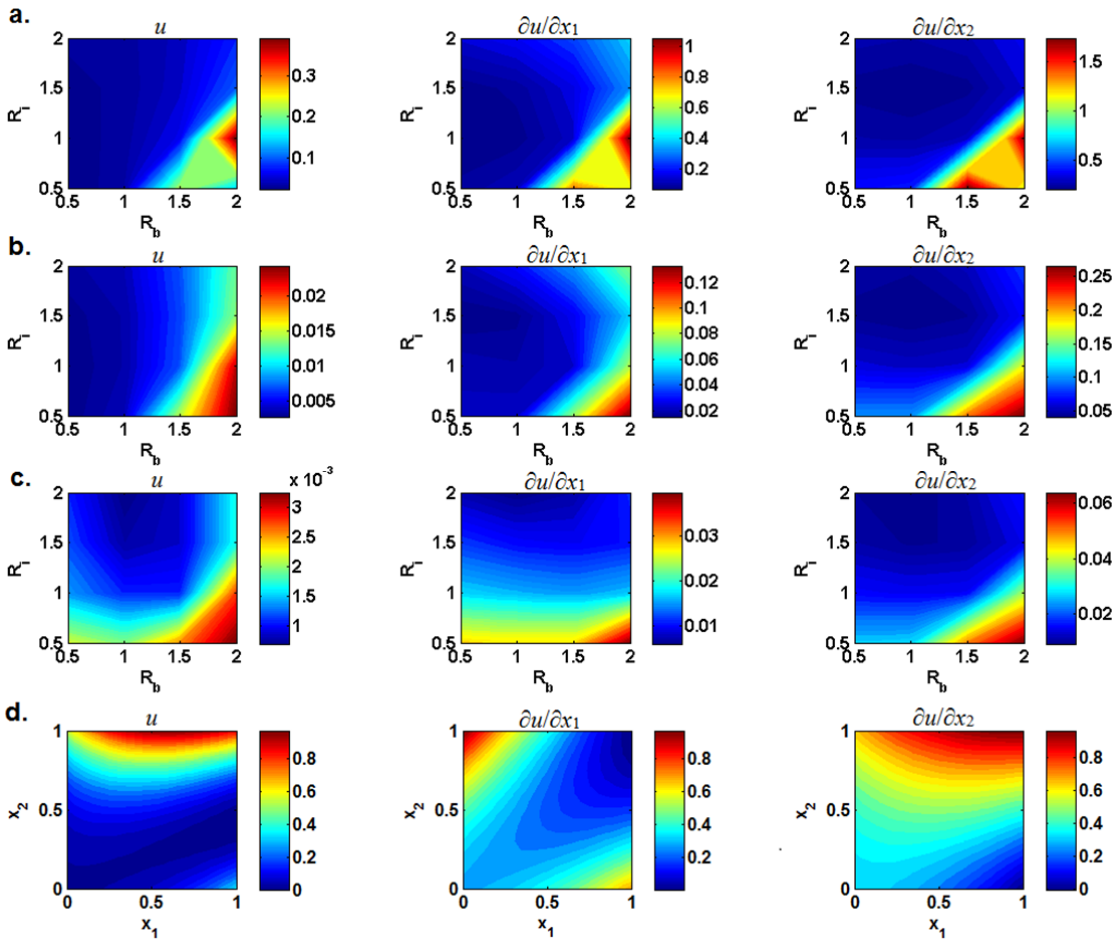

Figure 5: Contours of the RMS norm errors (%) of u, $\partial u/\partial x_1$ and $\partial u/\partial x_2$ obtained for (a) δx = 0.1, (b) δx = 0.05 and (c) δx = 0.025. Figure 5(d) plots the contours of u, $\partial u/\partial x_1$ and $\partial u/\partial x_2$.

5.1.2 Effects of Gauss points

The effects of the number of Gauss points on the performance of the anisotropic RBIE are investigated. Based on the results from the previous section, we set the radii of the interior and boundary subdomain to $2.0\delta x$ and $1.0\delta x$, respectively. Simulations were carried out using 75, 100, 125, 150 and 175 Gauss points. All other parameters were set to be the same as those employed in Section 5.1.1.

Figure 6 plots the variation of the RMS error of u, $\partial u/\partial x_1$ and $\partial u/\partial x_2$ against the number of Gauss points. When N_t is small, approximately 100 Gauss points were needed to obtain converged solution. However, these results are not meaningful due to their poor accuracy. By increasing the number of nodes, the number of Gauss points needed to attain convergence increased to 150. This is to ensure that the evaluations of the numerical integration in Eq. (15) are accurate. If the number of Gauss points is insufficient, then errors from the numerical integration will dominate, as indicated by the larger RMS error for N_t = 1681 using $N_g \leq 100$.

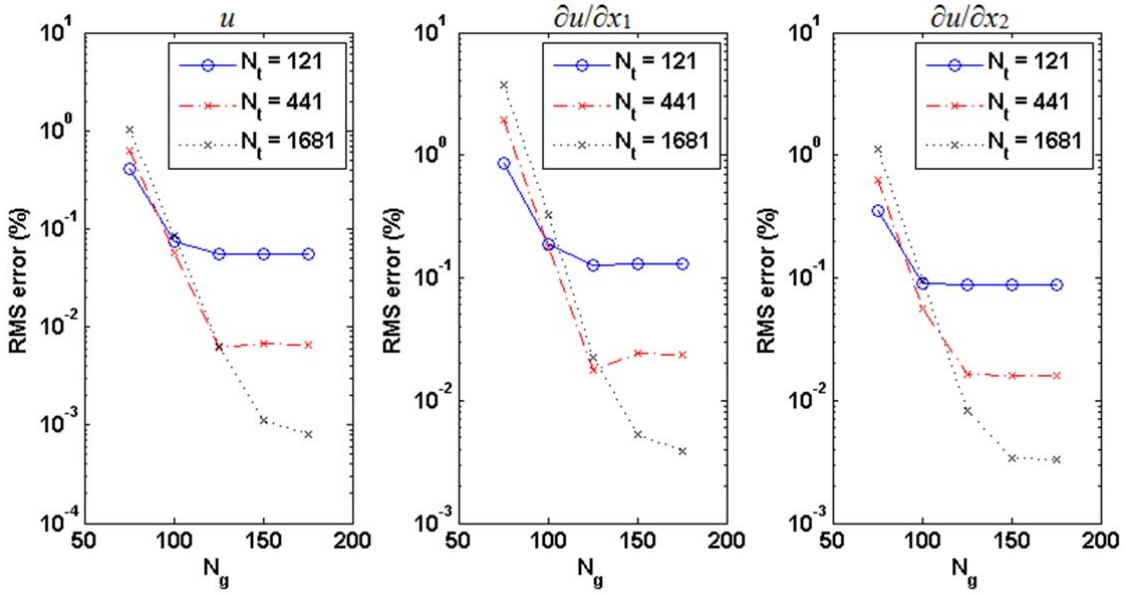

Figure 6: Variations of the RMS norm errors (%) of u, $\partial u/\partial x_1$ and $\partial u/\partial x_2$ against the number of Gauss points.

5.1.3 Effects of using geodesic distance

The reason for opting for the geodesic distance when defining the RBF has been detailed in Section 3.5. In this section, we investigate the importance of using the geodesic distance by comparing the results against those obtained using the Euclidean-based RBFs. For this purpose, we set the number of Gauss points to 150 and the radii of interior and boundary subdomains to be $2.0\delta x$ and $1.0\delta x$, respectively.

Table 1 compares the RMS error of u, $\partial u/\partial x_1$ and $\partial u/\partial x_2$ obtained using the geodesic- and the Euclidean-based RBFs. The results suggest that the algorithm employing the geodesic-based RBFs is on average, 1.6 times more accurate than those obtained using Euclidean-based RBFs. This is improvement is significant, which highlights the importance of adopting the geodesic distance instead of the Euclidean distance in defining the RBF when solving anisotropic problems.

Table 1: Comparisons of RMS errors (%) of u, $\partial u/\partial x_1$ and $\partial u/\partial x_2$ between the geodesic- and Euclidean-based RBFs.

N_t	u		$\partial u/\partial x_1$		$\partial u/\partial x_2$	
	Geodesic	Euclidean	Geodesic	Euclidean	Geodesic	Euclidean
121	0.0556	0.0975	0.1302	0.1868	0.0875	0.1595
441	0.0067	0.0130	0.0241	0.0300	0.0158	0.0254
1681	0.0011	0.0019	0.0053	0.0078	0.0034	0.0048

5.2 Test problem 2

As a second test problem, we consider an irregular-shaped domain, which is defined by:

$$r(\theta) = \frac{1}{n^2}\left[1 + 2n + n^2 - (n+1)\cos(n\theta)\right], \tag{22}$$

where r is the radius that depends on the angle θ (see Figure 7(a)) and n determines the number of rounded corners. For the purpose of this study, we have selected $n = 4$ and the resulting domain is shown in Figure 7(a). The coefficients of the anisotropic conductivity were chosen to be $k_{11} = 3$, $k_{22} = 2$ and $k_{12} = 1.5$. The following Dirichlet condition is prescribed along the boundary:

$$u(x_1, x_2) = \sin\left(\frac{x_2}{\sqrt{2}}\right)\cosh\left(\frac{2\sqrt{30}}{15}x_1 - \frac{\sqrt{30}}{10}x_2\right). \tag{23}$$

The exact solution across the boundary and interior of the solution domain is also represented by Eq. (23).

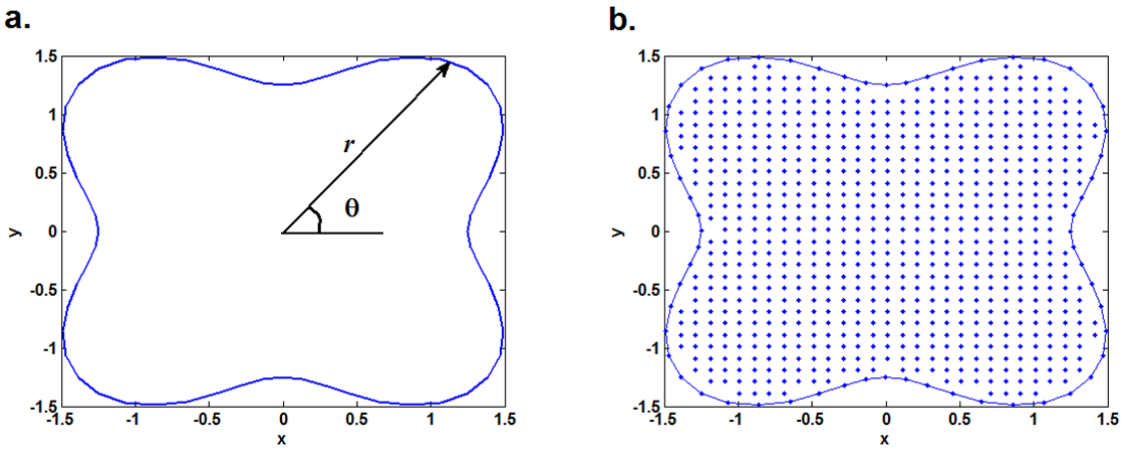

Figure 7: (a) Geometry of test problem 3 ($n = 4$) and (b) an example of meshless nodes distribution.

We set the radii of interior and boundary subdomains to be $2.0\delta x$ and $1.0\delta x$, respectively. The problem is solved by prescribing five different nodes distributions within the domain, namely $N_t = 145$, 225, 769, 1369 and 3093. A sample distribution of the collocated nodes across the solution domain is illustrated in Figure 7(b). It was found that for this problem, 60 Gauss points are sufficient to produce converged solutions. Simulations were carried out using the second and third order polyharmonic splines with second and third order polynomial augmentations, respectively.

Figure 8 plots the variation of RMS error of u, $\partial u/\partial x_1$ and $\partial u/\partial x_2$ against the total number of nodes used. In general, the accuracy of the numerical solution increases by one order of magnitude when the order of the RBF is increases from second to third. Using the third order RBF also increases the convergence rate of the numerical scheme.

Figure 9 compares the distribution of absolute error ($e_{abs} = |u_{\text{numerical}} - u_{\text{exact}}|$) of u, $\partial u/\partial x_1$ and $\partial u/\partial x_2$ between the second and third order RBFs obtained using $N_t = 3093$. The improvements in the numerical solution obtained by using the third order RBF are clearly elucidated.

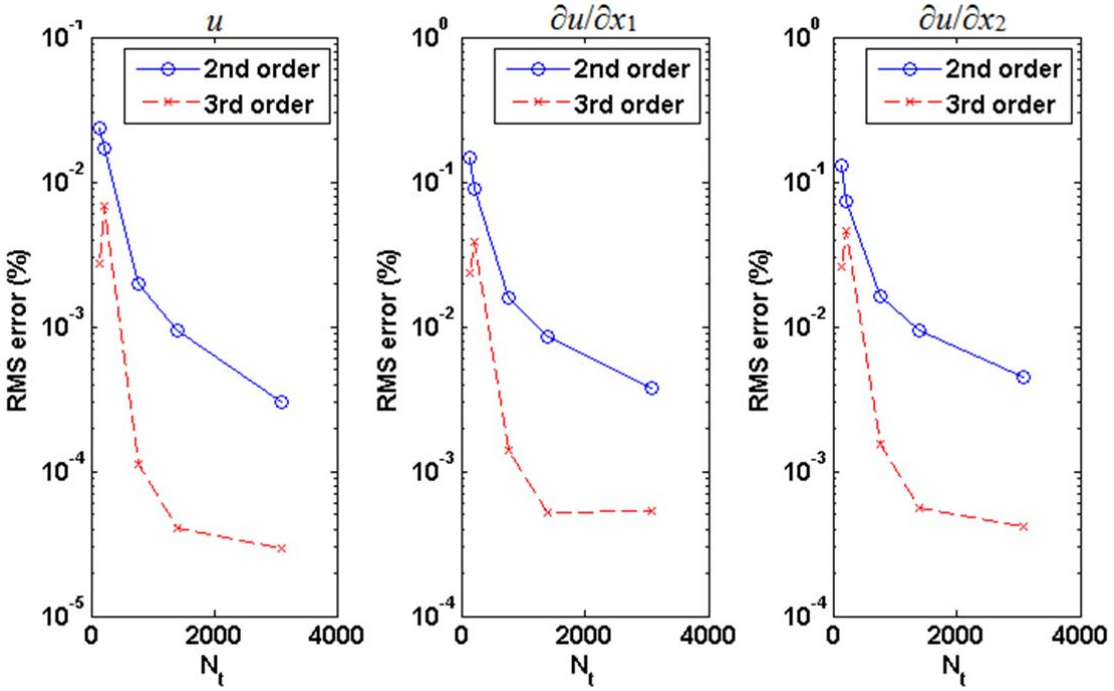

Figure 8: Plots of RMS error of u, $\partial u/\partial x_1$ and $\partial u/\partial x_2$ against the total number of nodes for test problem 2.

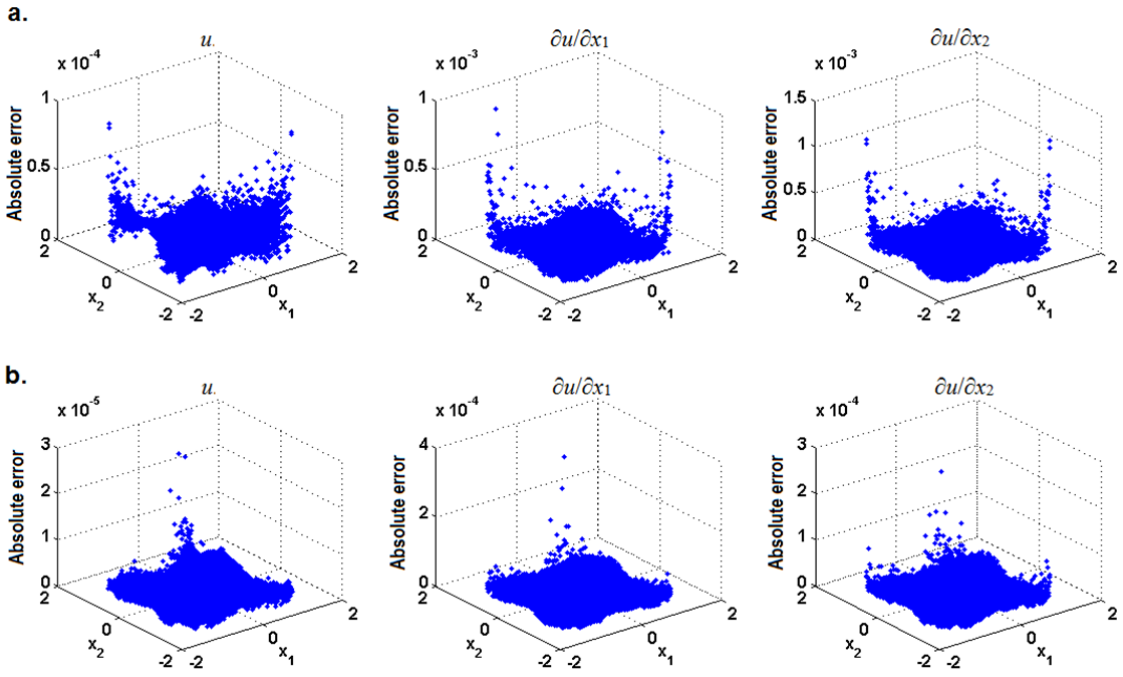

Figure 9: Distribution of absolute error of u, $\partial u/\partial x_1$ and $\partial u/\partial x_2$ in test problem 2 obtained using: (a) second and (b) third order RBFs.

6. Discussion

The accuracy and stability of the anisotropic RBIE were found to depend on the accuracy at which the influence coefficients are evaluated. This takes precedence over the total number of nodes used. This is the result of the large variation of the anisotropic fundamental solution over the subdomain boundary as both the strength of the material anisotropy increases and the subdomain radius becomes smaller. This problem does not exist when solving isotropic problems, where typical convergence behaviour is demonstrated in most cases [6].

The anisotropic fundamental solution and its spatial gradients also vary more greatly than the isotropic case. These larger variations suggest that more Gauss points are needed to compute more accurately the integrals in Eq. (15). In test problem 1, at least 150 Gauss points were needed in the numerical integration in order to achieve convergent numerical solutions. In other words, increasing the number of nodes in the simulation may not guarantee improved results if the calculations of the influence coefficients are not sufficiently accurate. In contrast, quadrature points as low as 10 have been reported to yield excellent results in isotropic RBIE [6]. Provided that sufficient Gauss points are used, the anisotropic RBIE can yield solutions that are accurate up to 4 decimal places.

One of the consequences of using large number of Gauss points in the numerical integration is the longer CPU time required. Table 2 presents the total CPU time of the anisotropic RBIE utilizing the second and third order RBFs for N_g = 10, 20, 40, 80 and 160. The data suggest that the CPU time increases exponentially as the number of Gauss points is doubled successively. For the two test problems considered here, the largest number of Gauss points needed is 150. Based on the tabulated data, the CPU time needed to solve anisotropic problems using the RBIE is still reasonably short. It is important to point out that the CPU time used in numerically calculating Eq. (15) is independent of the number of nodes used. These integrals are evaluated only once for the subdomains with the same radius.

The third order RBF requires a slightly longer CPU time than the second order RBF. The difference is due to the larger number of terms used in the accompanying polynomial augmentation. The difference appears to be negligible, however.

Table 2: Total CPU time (s) of the anisotropic RBIE with N_t = 961.

N_g	RBF	
	2^{nd} order	3^{rd} order
10	4.698	4.840
20	4.968	5.097
40	5.555	5.759
80	6.851	7.106
160	10.503	10.669

Errors from the numerical integration and problems with the extended CPU time can be avoided if alternative techniques to evaluate the integrals in Eq. (15) are available. In anisotropic BEM, integration of the anisotropic fundamental solution over a boundary element can be carried out analytically if the boundary elements are represented by a straight line [21, 22]. In RBIE, analytical evaluation of the integrals along the circular boundary is complicated by the presence of the RBF term $f(x_1,x_2;x_1^{(k)},x_2^{(k)})$.

Some researchers have used the BEM along with a transformation approach to solve anisotropic problems in order to avoid having to deal with anisotropic fundamental solutions [23-26]. In this approach, the Cartesian axes are re-oriented into the principal axes such that the governing anisotropic potential equation becomes the Laplace equation. The problem is then solved using the BEM in the transformed (principal) axes. This transformation technique

can be used with the RBIE; however, it is noteworthy that for problems with strong anisotropy, the transformation produces a domain that is severely distorted. For the square domain considered in Section 5.1, the domain in the transformed space becomes extremely thin. Consequently, while the effects of anisotropy on the sensitivity of the influence coefficients is inconsequential in the transformed space, one would have to deal with an extremely slender domain, which is problematic and very difficult to solve.

The numerical experiments showed that for $\delta x = 0.025$, the optimum interior and boundary subdomain radii were $2.0\delta x$ and $1.0\delta x$, respectively. These values are different from the case when solving isotropic problems ($1.0\delta x$ for interior subdomains and $0.1\delta x$ for boundary subdomains), largely because the variations of the fundamental solution and its spatial derivatives depend on the size of the subdomain. For the set of nodes where $\delta x = 0.025$, the RMS errors are also less sensitive to the subdomain radius, suggesting that choosing subdomain sizes that deviate from their optimal values have very little impact on the accuracy of the numerical method.

It is possible to generate the subdomains by setting the radius to a constant so that the dependence on the number of nodes is eliminated. However, this approach does not guarantee more accurate results because the majority of the interpolation points will be located inside the subdomain when the number of nodes is increased. This scenario is shown in Figure 10. In Figure 10 (a), the radius of the subdomain is scaled according to $2.0\delta x$. With $N_a = 25$, the points selected for the RBF interpolation are both located inside and outside of the subdomain, as depicted by the dashed-red square in Figure 10 (a).

Conversely, if the subdomain size is fixed, then increasing the number of nodes will result in all the RBF points lying inside the subdomain (Figure 10 (b)). This can introduce errors to the numerical solution, since the method is similar to extrapolating the unknown functions along the subdomain boundary using only nodes inside the subdomain. This problem can be alleviated by increasing the number of interpolation points, as shown by the green dashed-dotted box in Figure 10 (b). However, this approach will increase the computational time and may not guarantee better results due to the additional error introduced when inversing the larger system matrix (see Eq. (10)).

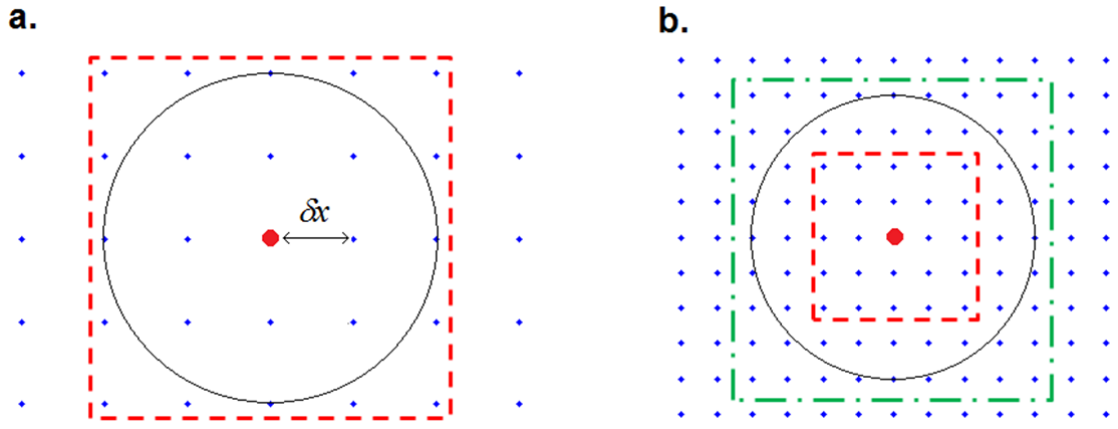

Figure 10: (a) Interior subdomain having radius $2.0\delta x$ and (b) interior subdomain at a fixed value with increased number of nodes. The red dot represents the centre of subdomain, while the blue points inside the dashed red square represent the nodes used in the RBF interpolations.

The analyses and the numerical results presented in Section 5 have been carried out and obtained using the standard formulation, which computes the unknown potential and its

spatial gradients at each node. As pointed out in Section 2, an alternative formulation may be derived that solves for the potential and the component of fluxes q_1 and q_2:

$$q_1(x_1,x_2) = k_{11}\frac{\partial u(x_1,x_2)}{\partial x_1} + k_{12}\frac{\partial u(x_1,x_2)}{\partial x_2}, \tag{23a}$$

$$q_2(x_1,x_2) = k_{12}\frac{\partial u(x_1,x_2)}{\partial x_1} + k_{22}\frac{\partial u(x_1,x_2)}{\partial x_2}. \tag{23b}$$

In order to test the performance of the alternative formulation, we repeated the simulations for test problem 2 using the same parameters as those used in Section 5.2. Figure 11 compares the RMS error of u, $\partial u/\partial x_1$ and $\partial u/\partial x_2$ obtained using the standard and alternative formulations. The accuracies of both the standard and alternative formulations in calculating u were indistinguishable. The standard formulation calculated $\partial u/\partial x_1$ and $\partial u/\partial x_2$ more accurately, albeit insignificantly, than the alternative formulation in calculating q_1 and q_2. Nevertheless, direct comparison between the standard and alternative formulations is difficult, since q_1 and q_2 are themselves, functions of both $\partial u/\partial x_1$ and $\partial u/\partial x_2$, see Eq. (23).

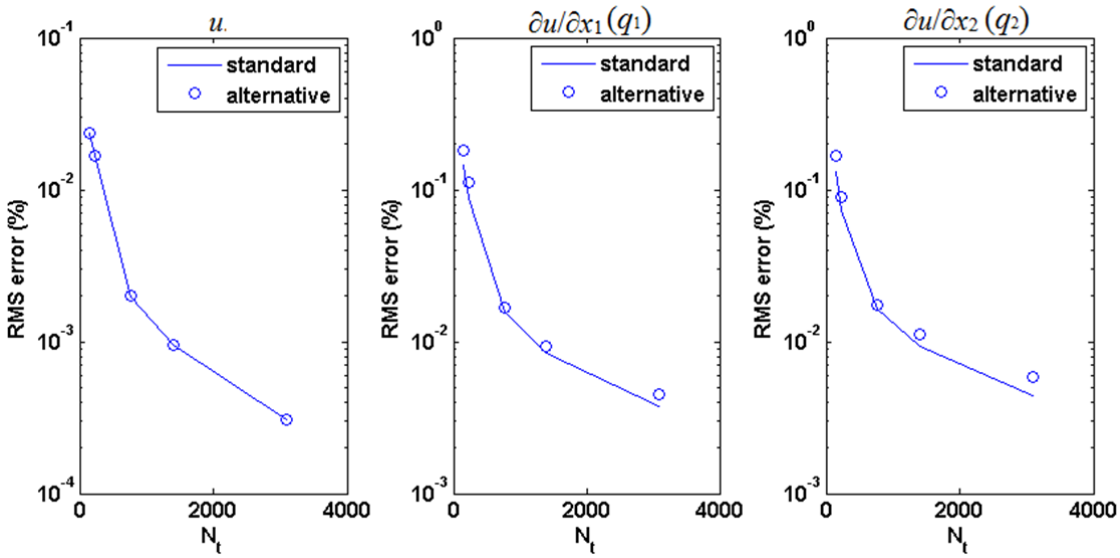

Figure 11: Comparison of RMS error of u, $\partial u/\partial x_1$ and $\partial u/\partial x_2$ between the standard and the alternative formulations.

The plots in Figure 11 suggest that both the standard and alternative formulations are capable of producing comparable numerical results and that the difference in the level of accuracy in both formulations have little influence over the choice of which formulation to use in a particular problem. The merit of the alternative formulation can be appreciated when solving practical engineering problems, where the fluxes on the boundary known instead of the spatial potential gradients. For instance, in heat transfer problems, heat flux is usually known at the boundary instead of temperature gradients.

7. Conclusions

The RBIE has been derived for the first time to solve potential problems involving material anisotropy. The performance of the numerical method was tested by solving some numerical benchmarks. Unlike the isotropic case, solutions of anisotropic problems using the RBIE are

less straightforward. The variations of the fundamental solution and its spatial derivatives were found to depend on both the material anisotropy and the size of the subdomain, which affected the optimum computational parameters.

Numerical experiments indicated that for the problems considered in this paper, the optimum radius was found to be $2.0\delta x$ for subdomains at the interior and $1.0\delta x$ for subdomains at the boundary with $\delta x = 0.025$. It was also determined that at this δx, the accuracy of the numerical algorithm is less sensitive towards the changes in the subdomain radius. This is true provided that the number of Gauss points used is sufficient to accurately capture the variation of the fundamental solution and its spatial gradients along the subdomain boundary. The importance of using the geodesic distance to define the RBF is also demonstrated. Comparisons between the second and third order polyharmonic splines showed that the third order spline is one order more accurate than the second order spline. The increase in CPU time as a result from implementing the third order spline is negligible.

One of the key aspects when implementing the anisotropic RBIE is the accurate evaluation of the influence coefficients. This appears to be the most significant criterion and supersedes the increase in the number of nodes used. In order to accurately evaluate the influence coefficients, large number of Gauss points is needed for the numerical integration, which leads to considerable increases in the total CPU time. This drawback may be avoided if analytical or semi-analytical solutions of the integrals in Eq. (15) can be derived and is the subject of future investigations.

An alternative formulation of the anisotropic RBIE, which allows for the potential and fluxes in the x_1- and x_2-directions to be calculated was also presented. There were no significant differences in the accuracies between the standard and alternative formulations. The alternative formulation is suggested to be more practical for solving problems where fluxes are prescribed as the boundary conditions instead of the potential gradients.

Appendix A

For simplicity, we define the geodesic distance as:

$$\Re = \sqrt{s_{11}(x_1-\xi_1)^2 + 2s_{12}(x_1-\xi_1)(x_2-\xi_2) + s_{22}(x_2-\xi_2)^2} \tag{A1}$$

The fundamental solution of the anisotropic Laplace equation and its first and second order derivatives are given by:

$$\Phi = \frac{|s_{ij}|^{\frac{1}{2}}}{2\pi}\ln(\Re), \tag{A2}$$

$$\frac{\partial\Phi}{\partial x_1} = -\frac{\partial\Phi}{\partial\xi_1} = \frac{|s_{ij}|^{\frac{1}{2}}}{2\pi}\left\{\frac{s_{11}(x_1-\xi_1)+s_{12}(x_2-\xi_2)}{\Re^2}\right\}, \tag{A3}$$

$$\frac{\partial\Phi}{\partial x_2} = -\frac{\partial\Phi}{\partial\xi_2} = \frac{|s_{ij}|^{\frac{1}{2}}}{2\pi}\left\{\frac{s_{12}(x_1-\xi_1)+s_{22}(x_2-\xi_2)}{\Re^2}\right\}, \tag{A4}$$

$$\Theta = \frac{\partial\Phi}{\partial n^+} = \frac{|s_{ij}|^{\frac{1}{2}}}{2\pi}\left\{\frac{\kappa_1[s_{11}(x_1-\xi_1)+s_{12}(x_2-\xi_2)]+\kappa_2[s_{12}(x_1-\xi_1)+s_{22}(x_2-\xi_2)]}{\Re^2}\right\}, \tag{A5}$$

$$\frac{\partial^2\Phi}{\partial\xi_1\partial x_1}=\frac{|\,s_{ij}\,|^{\frac{1}{2}}}{2\pi}\left\{-\frac{s_{11}}{\Re^2}+\frac{2\left[s_{11}(x_1-\xi_1)+s_{12}(x_2-\xi_2)\right]^2}{\Re^4}\right\}, \tag{A6}$$

$$\frac{\partial^2\Phi}{\partial\xi_2\partial x_1}=\frac{|\,s_{ij}\,|^{\frac{1}{2}}}{2\pi}\left\{-\frac{s_{12}}{\Re^2}+\frac{2\left[s_{11}(x_1-\xi_1)+s_{12}(x_2-\xi_2)\right]\left[s_{12}(x_1-\xi_1)+s_{22}(x_2-\xi_2)\right]}{\Re^4}\right\}, \tag{A7}$$

$$\frac{\partial^2\Phi}{\partial\xi_1\partial x_2}=\frac{|\,s_{ij}\,|^{\frac{1}{2}}}{2\pi}\left\{-\frac{s_{12}}{\Re^2}+\frac{2\left[s_{11}(x_1-\xi_1)+s_{12}(x_2-\xi_2)\right]\left[s_{12}(x_1-\xi_1)+s_{22}(x_2-\xi_2)\right]}{\Re^4}\right\}, \tag{A8}$$

$$\frac{\partial^2\Phi}{\partial\xi_2\partial x_2}=\frac{|\,s_{ij}\,|^{\frac{1}{2}}}{2\pi}\left\{-\frac{s_{22}}{\Re^2}+\frac{2\left[s_{12}(x_1-\xi_1)+s_{22}(x_2-\xi_2)\right]^2}{\Re^4}\right\}, \tag{A9}$$

Appendix B

In this appendix, we derive the alternative formulation of the anisotropic RBIE which solves for the potential and the components of flux instead of the spatial gradients. We begin by defining the normal component of the flux q_n, which may be written as:

$$q_n(x_1,x_2)\equiv\frac{\partial u(x_1,x_2)}{\partial n^+}=n_1(x_1,x_2)q_1(x_1,x_2)+n_2(x_1,x_2)q_2(x_1,x_2), \tag{B1}$$

where

$$q_1(x_1,x_2)=k_{11}\frac{\partial u(x_1,x_2)}{\partial x_1}+k_{12}\frac{\partial u(x_1,x_2)}{\partial x_2}, \tag{B2a}$$

$$q_2(x_1,x_2)=k_{12}\frac{\partial u(x_1,x_2)}{\partial x_1}+k_{22}\frac{\partial u(x_1,x_2)}{\partial x_2}. \tag{B2b}$$

Substituting the expressions above into the integral equation for potential (Eq. (4)) yields:

$$\begin{aligned}u(\xi_1^{(i)},\xi_2^{(i)})=\int_{\Gamma_i}\Big[&u(x_1,x_2)\Theta(x_1,x_2;\xi_1^{(i)},\xi_2^{(i)})-n_1(x_1,x_2)\Phi(x_1,x_2;\xi_1^{(i)},\xi_2^{(i)})q_1(x_1,x_2)\\&-n_2(x_1,x_2)\Phi(x_1,x_2;\xi_1^{(i)},\xi_2^{(i)})q_2(x_1,x_2)\Big]\mathrm{d}s(x_1,x_2),\end{aligned} \tag{B3}$$

Differentiating Eq. (B3) with respect to ξ_1 and ξ_2 and by making use of the following relationship:

$$q_1(\xi_1,\xi_2)=k_{11}\frac{\partial u(\xi_1,\xi_2)}{\partial\xi_1}+k_{12}\frac{\partial u(\xi_1,\xi_2)}{\partial\xi_2}, \tag{B4a}$$

$$q_2(\xi_1,\xi_2)=k_{12}\frac{\partial u(\xi_1,\xi_2)}{\partial\xi_1}+k_{22}\frac{\partial u(\xi_1,\xi_2)}{\partial\xi_2}, \tag{B4b}$$

one obtains:

$$q_1^{(i)} = \int_{\Gamma_i} \left[\left(k_{11} \frac{\partial \Theta^{(i)}}{\partial \xi_1} + k_{12} \frac{\partial \Theta^{(i)}}{\partial \xi_2} \right) \frac{\partial \Theta^{(i)}}{\partial \xi_1} u - n_1 \left(k_{11} \frac{\partial \Phi^{(i)}}{\partial \xi_1} + k_{12} \frac{\partial \Phi^{(i)}}{\partial \xi_2} \right) q_1 \right.$$
$$\left. - n_2 \left(k_{11} \frac{\partial \Phi^{(i)}}{\partial \xi_1} + k_{12} \frac{\partial \Phi^{(i)}}{\partial \xi_2} \right) q_1 \right] \mathrm{d}s(x_1, x_2), \tag{B5}$$

$$q_2^{(i)} = \int_{\Gamma_i} \left[\left(k_{12} \frac{\partial \Theta^{(i)}}{\partial \xi_1} + k_{22} \frac{\partial \Theta^{(i)}}{\partial \xi_2} \right) \frac{\partial \Theta^{(i)}}{\partial \xi_1} u - n_1 \left(k_{12} \frac{\partial \Phi^{(i)}}{\partial \xi_1} + k_{22} \frac{\partial \Phi^{(i)}}{\partial \xi_2} \right) q_1 \right.$$
$$\left. - n_2 \left(k_{12} \frac{\partial \Phi^{(i)}}{\partial \xi_1} + k_{22} \frac{\partial \Phi^{(i)}}{\partial \xi_2} \right) q_1 \right] \mathrm{d}s(x_1, x_2), \tag{B6}$$

where the fundamental solution and its first and second order derivatives are given as in Appendix A. As in the standard formulation, the field variables u, q_1 and q_2 may be expressed in terms of the values at the surrounding nodes by using RBF interpolations. Detailed derivation following these steps will not be presented as they are identical to those adopted in the standard formulation.

Implementation of the alternative formulation is slightly different from the standard formulation. For nodes that are located at the interior and at the boundary where the Dirichlet condition is prescribed, the procedures are the same as in the standard formulation. When the collocation node is at the boundary where the Neumann condition is prescribed, the two cases adopted in the standard formulation is also applicable to the alternative formulation. However, instead of checking for the conditions of $|\kappa_1|$ and $|\kappa_2|$, the conditions are checked for $|n_1|$ and $|n_2|$ and Eq. (B1) is used to eliminate one of q_1 or q_2.

References

1. Bear J, Cheng AHD, Modelling groundwater flow and contaminant transport, Springer, London, 2010.
2. Erbertseder K, Reichold J, Flemisch B, Jenny P, Helmig R, A coupled discrete/continiuum model for describing cancer-therapeutic transport in the lung. PLOS One, 2012, 7(3): e31966. doi:10.1371/journal.pone.0031966.
3. Kocks UF, Texture and anisotropy: preferred orientations in polycrystals and their effect on materials properties. Cambridge University Press, Cambridge, 2000.
4. Guenneau S, Amra C, Veynante D, Transformation thermodynamics: cloaking and concentrating heat flux. Optics Express, 2012; 20:8207-8218.
5. Popov V, Bui TT, A meshless solution to two-dimensional convection-diffusion problems. Engineering Analysis with Boundary Elements, 2010; 34:680–689.
6. Ooi EH, Popov V, An efficient implementation of the radial basis integral equation method. Engineering Analysis with Boundary Elements, 2012; 36:716–726.
7. Ooi EH, Popov V, Meshless solution of axisymmetric convection-diffusion equation: a comparison between two alternative RBIE implementations. Engineering Analysis with Boundary Elements, 2013; 37: 719-727.

8. Ooi EH, Popov V, Numerical study of influence of nanoparticle shape on the natural convection in Cu-water nanofluid. International Journal of Thermal Sciences, 2013; 65: 178-188.
9. Ooi EH, Popov V, Dogan H, Three dimensional solution for acoustic and transport problems using the radial basis integral equation method. Applied Mathematics and Computations, 2012; 218: 9470-9488.
10. Clements DL, Boundary value problems governed by the second order elliptic systems. Pitman, London, 1981.
11. Chang YP, Kang CS, Chen DJ, The use of fundamental green's functions for the solution of problems of heat conduction in anisotropic media. International Journal of Heat and Mass Transfer, 1973; 16: 1905-1918.
12. Cheng AHD, Particular solutions of Laplacian, Helmholtz-type, and polyharmonic operators involving higher order radial basis functions, Engineering Analysis with Boundary Elements, 2000; 24:531–538.
13. Dogan H, Popov V, Ooi EH, The radial basis integral equation method for 2D Helmholtz equation, Engineering Analysis with Boundary Elements, 2012; 36: 934-943.
14. Ooi EH, Popov V, Meshless solution of two-dimensional incompressible flow problems using the radial basis integral equation method. Applied Mathematical Modelling, 2013; 37: 8985-8998.
15. Cheng AHD, Multiquadric and its shape parameter-A numerical investigation of error estimate, condition number, and round-off error by arbitrary precision computation. Engineering Analysis with Boundary Elements, 2012; 36: 220-239.
16. Young DL, Jane SC, Lin CY, Chiu CL, Chen KC, Solutions of 2D and 3D Stokes laws using multiquadrics method. Engineering Analysis with Boundary Elements, 2004; 28: 1233-1243.
17. Bayona V, Moscoso M, Kindelan M, Gaussian RBF-FD weights and its corresponding local truncation errors. Engineering Analysis with Boundary Elements, 2012; 36: 1361-1369.
18. Dehghan M, Abbaszadeh M, Mohebbi A, The numerical solution of nonlinear high dimensional generalized Benjamin-Bona-Mahony-Burgers equation via the meshless method of radial basis functions. Computer and Mathematics with Applications, 2014; 68: 212-237.
19. Ang WT, Clements DL and Vahdati N, A dual-reciprocity boundary element method for a class of elliptic boundary value problems for nonhomogeneous anisotropic media, Engineering Analysis with Boundary Elements, 2003; 27: 49-55.
20. Partridge P.W., Towards criteria for selecting approximating functions in the dual reciprocity method. Engineering Analysis with Boundary Elements, 2000, 24: 519-529.
21. Mera NS, Elliott L, Ingham DB, Lesnic D, The boundary element solution of the Cauchy steady heat conduction problem in an anisotropic medium. International Journal for Numerical Methods in Engineering, 2000; 49: 481-499.
22. Mera NS, Elliott L, Ingham DB, Lesnic D, A comparison of boundary element method formulations for steady state anisotropic heat conduction problems. Engineering Analysis with Boundary Elements, 2001; 25: 115-128.
23. Laef O, Ligget J, Liu PF, BIEM solutions to combinations of leaky, layered, confined, unconfined, nonisotropic aquifers. Water Resource Research, 1981; 17: 1431-1444.
24. Ligget J, Liu PF, The boundary integral equation method for porous media flow. London: George Allen and Uwin Ltd, 1983.

25. Rafiezadeh K, Ataie-Ashtiani B, Three dimensional flow in anisotropic zoned porous media using boundary element method. Engineering Analysis with Boundary Elements, 2012; 36: 802-824.
26. Rafiezadeh K, Ataie-Ashtiani B, Seepage analysis in multi-domain general anisotropic media by three-dimensional boundary elements. Engineering Analysis with Boundary Elements, 2013; 37: 527-541.